

Magnetic order in a coherent two-dimensional Kondo lattice

Wen Wan¹, Rishav Harsh¹, Antonella Meninno^{2,3}, Paul Dreher¹, Sandra Sajan¹, Ion Errea^{1,2,3}, Fernando de Juan^{*,1,4} and Miguel M. Ugeda^{*,1,2,4}

¹*Donostia International Physics Center (DIPC), Paseo Manuel de Lardizábal 4, 20018 San Sebastián, Spain.*

²*Centro de Física de Materiales, Paseo Manuel de Lardizábal 5, 20018 San Sebastián, Spain.*

³*Departamento de Física Aplicada, Escuela de Ingeniería de Gipuzkoa, University of the Basque Country (UPV/EHU), Plaza Europa 1, 20018 San Sebastián, Spain.*

⁴*Ikerbasque, Basque Foundation for Science, 48013 Bilbao, Spain.*

* Corresponding authors: fernando.dejuan@dipc.org and mmugeda@dipc.org

Abstract

Kondo lattices are ideal testbeds for the exploration of heavy-fermion quantum phases of matter. While our understanding of Kondo lattices has traditionally relied on complex bulk f -electron systems, transition metal dichalcogenide heterobilayers have recently emerged as simple, accessible and tunable 2D Kondo lattice platforms where, however, their ground state remains to be established. Here we present evidence of coherent magnetism in the 1T/1H-TaSe₂ heterobilayer by means of scanning tunneling microscopy/spectroscopy at 340 mK. Our measurements reveal the existence of two symmetric electronic resonances around the Fermi energy, a hallmark of coherence in the spin lattice. Spectroscopic imaging locates both resonances at the central Ta atom of the charge density wave of the 1T phase, where the localized magnetic moment is held. Furthermore, the evolution of the electronic structure with the magnetic field reveals a non-linear increase of the energy separation between the electronic resonances. Aided by *ab initio* and auxiliary-fermion mean-field calculations, we demonstrate that this behavior is inconsistent with a fully screened Kondo lattice, and originates instead from a ground state with magnetic order mediated by conduction electrons. The manifestation of magnetic coherence in TMD-based 2D Kondo lattices enables the exploration of magnetic quantum criticality, Kondo breakdown transitions and unconventional superconductivity in the strict two-dimensional limit.

The complexity of the Kondo lattice problem is best appreciated in comparison with the relative simplicity of that involving a single Kondo impurity. At temperatures below T_K , a magnetic impurity coupled to a metal with Kondo exchange coupling J_K forms a singlet with the conduction electrons and becomes screened. In a periodic array of such impurities, the magnetic moments also develop independent singlets around T_K . However, as the temperature is further lowered below a coherence scale T^* , the magnetic moments start coupling with each other, and a coherent heavy fermion state forms with non-Fermi liquid properties. A microscopic understanding of the ground state of this coherent Kondo lattice remains a central problem in condensed matter physics. The phase diagram first proposed by Doniach¹ (Fig. 1) highlights the core of the problem, where the competition between Kondo-type and Ruderman–Kittel–Kasuya–Yosida (RKKY) interactions between moments drives the system to either a Kondo paramagnet or to a magnetic state. Understanding the nature and possible types of zero-temperature quantum critical points between such phases and their influence in phenomena like non-Fermi liquid behavior, the Kondo breakdown and fluctuation-mediated superconductivity remains a great challenge in the field. Experimentally, the understanding of these fascinating problems has traditionally been hindered by the complexity and lack of tunability of the *f*-electron compounds like those based in Ytterbium² or Cerium³.

The observation of the Kondo effect in transition metal dichalcogenide (TMD) heterobilayers formed by vertical stacks of T- and H-type monolayers has recently opened a new, simple and accessible platform to design artificial Kondo lattices^{4,5} in strict two-dimensions. In these systems, the 1T monolayer develops a $\sqrt{13}\times\sqrt{13}$ CDW known as the Star-of-David (SoD) pattern, which leaves a single unpaired electron near the Fermi energy (E_F) that forms an effective impurity flat band. The residual Hubbard interaction in this flat band leads to an array of local moments and to a magnetic Mott insulating state. When the 1T layer is stacked onto a metal, the hybridization of the impurity band with the Fermi surface enables the Kondo effect. A narrow Kondo peak has been observed in these T/H heterobilayers of TaSe₂, TaS₂ and NbSe₂ with T_K in the range 18-57 K, providing compelling evidence of the formation of local moments⁴⁻⁷. However, lower-temperature evidence for any coherence behavior of the Kondo lattice remains sorely lacking, and fundamental questions such as the ground state of these compounds in the Doniach diagram remain unanswered.

In this work, we address this problem by performing high-resolution scanning tunneling microscopy/spectroscopy (STM/STS) experiments at 340 mK in the prototype 1T/1H-heterostructure and demonstrate coherent behavior beyond single moment physics, in the form of a split Kondo peak whose separation increases non-linearly upon an out-of-plane magnetic field (B_z). Rationalizing our observations in terms of a periodic Anderson model with parameters extracted from *ab initio*

calculations, we argue that our results are clear evidence of a magnetic phase of the coherent Kondo lattice with in-plane magnetic order.

Our experiments were carried out in high-quality 1T/1H heterobilayers of TaSe₂ grown on epitaxial bilayer graphene (BLG) on 6H-SiC(0001), as sketched in Fig. 1a. The vertical 1T/1H heterobilayer is naturally formed during the growth of few-layer TaSe₂ as both polytypes coexist due to their similar formation energies⁸ (see supplementary materials (SM) for growth details and morphology). The robust commensurate charge density wave (CDW) developed in bulk 1T-TaSe₂ is also easily distinguished in STM images in the monolayer limit as a ($\sqrt{13}\times\sqrt{13}$)R13.9° triangular superlattice (yellow rhombus in Fig. 2a). Each bright spot in the superlattice corresponds to a cluster of 13 Ta atoms (the SoD) where an individual magnetic moment develops due to the presence of an unpaired electron.

To study the electronic structure of 1T-TaSe₂ on 1H-TaSe₂, we carried out STS measurements at 4.2 K and 0.34 K. dI/dV spectra ($dI/dV \propto \text{LDOS}$) taken on this heterostructure at 4.2 K (Fig. 2b) are dominated by a prominent single peak centered at the Fermi level (E_F) with typical width of 10 meV. The existence of this peak feature, previously reported for single-layer 1T-TaS₂ and 1T-TaSe₂, has been ascribed to a Kondo resonance due to the screening of the SoD magnetic moments by the underlying metal substrate (1H phase)^{4,5,7,9}. This peak is flanked by two broader peaks that can be identified as the lower (upper) Hubbard bands, which yield an experimental measure of the Hubbard repulsion of $U = 208 \pm 4$ meV (see SM). As the temperature of the 1T/1H heterostructure is lowered below 4.2 K, the sharp peak feature at E_F , however, is better resolved spectroscopically and two symmetric peaks with respect to E_F are observed, as shown in the representative dI/dV spectrum taken at our base temperature of $T = 0.34$ K in Fig. 2c. It is worth mentioning that the gradual emergence of these two peaks is not due to a T-dependent process but rather due to an improvement of energy resolution in STS as T is lowered (see SM for the full evolution with T). This double-peak feature is in contrast with the 1T-TaS₂ case, where only one peak appears at sub-kelvin temperatures at zero magnetic field⁵.

To gain further knowledge about the low-lying electronic structure of the 1T/1H heterostructure, we carried out spatially resolved measurements at 0.34 K in several nm-sized regions, one of which is shown in Fig. 3a. Fig. 3b shows three dI/dV spectra taken at the center of three neighboring clusters (colored dots in Fig. 3a), which reveal that the separation between the two peaks (Δ) presents significant variations. We have quantified these variations by spatially mapping Δ in this region (Fig. 3c) from a 40 x 40 dI/dV grid. As seen, Δ mostly varies between SoD clusters, being

largely constant inside each of them. Fig. 3d shows the resulting histogram of Δ , which shows a mean value of $\bar{\Delta} = 1.2 \pm 0.2 \text{ mV}$. Very similar values were found in all the regions studied.

We have also characterized the spatial extension of the two electronic peaks by measuring atomically resolved conductance maps (constant height) of the 1T/1H heterostructure (Figs. 3e-g). Figs. 3e and 3g show two conductance maps taken consecutively at $\pm 1 \text{ mV}$ in the same region shown in Fig. 2f. Both conductance maps are nearly identical and reveal that the intensity of these two peaks is mostly localized on the three Se atoms directly bonded to the Ta atom at the center of the SoD, although some residual intensity lies on the second Se neighbors. This is in good agreement with the expected location of the unpaired electron that gives rise to a net magnetic moment.

In order to elucidate the origin of this two-peak feature, we have performed a thorough characterization of the electronic structure subject to external magnetic fields (out of plane). Figure 3a shows a representative series of dI/dV spectra within $\pm 25 \text{ mV}$ acquired consecutively as B_z is swept up to 11 T. The most obvious effect of B_z on the LDOS is the gradual shift of both peaks from E_F , which leads to an increase of Δ with B_z . In parallel to this energy shift, the LDOS is gradually depleted around E_F and the intensity of the peaks diminish with B_z , as shown in the zoom-in of Fig. 4b and plots in Fig. 4c. Beyond these changes, the electronic structure for larger energies seems to be nearly unperturbed by the magnetic field. To confirm that no further features appear in the low-energy electronic structure upon the application of B_z , high-resolution dI/dV spectra ($\sim 30 \mu\text{V}/\text{point}$) were systematically taken around the peaks maxima in different regions in the 0–11 T range. As shown in Fig. 4d, no further structures appear within our energy resolution ($\sim 80 \mu\text{eV}$ at $T = 0.34 \text{ K}$) and only two peaks remain visible at high magnetic fields.

From our B -dependent STS measurements such as the dI/dV sets of Fig. 5a and 5d, we have quantified the evolution of the peaks' maxima with B_z . Figure 5a shows a typical plot of the peaks' separation Δ as a function of B_z . We consistently find that the evolution of Δ with B_z has two differentiated regimes: a strict linear dependence of Δ for $B_z \gtrsim 0.5 \text{ T}$ (linear fit in red, see SM) preceded by a non-linear regime at lower B_z fields (region shaded in green). The linear dependence of Δ with B_z is attributed to a Zeeman splitting with a Landé g -factor of $g = 4.3 \pm 0.4$. Fig. 5b shows a zoom-in of the low- B field regime, where $\Delta(B_z)$ gradually deviates from the linear dependence (beyond the confidence band depicted in grey) below 0.5 T to ultimately reach a deviation of $|S| = 0.17 \text{ mV}$ at $B_z = 0 \text{ T}$ from the linear behavior. Another important observation regarding the $\Delta(B_z)$ dependence is that this behavior is independent from the polarity of the magnetic field ($\pm B_z$). This is shown in Fig. 5c (zoom-in in Fig. 5d), where B_z was swept in between $\pm 11 \text{ T}$. As seen, Δ shows an

equal behavior with B_z at both polarities, which allow us to rule out hysteresis phenomena and non-symmetric behavior. This symmetric two-regime behavior of $\Delta(B_z)$ has been found in most of the SoD clusters where the B_z -dependent STS was measured, from which we can extract an average Δ deviation at zero field of $|S| = 0.15 \pm 0.02$ mV (see histogram in Fig. 5e) and an average field for the non-linear to linear transition at $\overline{B_T} = 0.45 \pm 0.07$ T (see SM for other dI/dV sets).

The observation of a split Kondo peak reveals that the coherence regime of the Kondo lattice has been reached. Further analysis is nevertheless required to determine the nature of its ground state, and where it lies in the Doniach phase diagram. This analysis can be framed in terms of a periodic Anderson model, where a periodic array of Anderson impurities corresponding to the 1T SoD moments is coupled to the folded metallic bands of the 1H layer

$$H = \sum_{i,j \in H, \sigma} t_{ij} c_{i\sigma}^+ c_{j\sigma} + \sum_{i \in T, \sigma} [\epsilon_0 f_{i\sigma}^+ f_{i\sigma} + V(c_{i\sigma}^+ f_{i\sigma} + f_{i\sigma}^+ c_{i\sigma}) + U n_{f\uparrow, i} n_{f\downarrow, i}].$$

Here $c_{i\sigma}^+$ creates an electron with spin σ in metal site i on the H layer, $f_{i\sigma}^+$ creates an electron on the SoD Wannier orbital i on the T layer with $n_{f\sigma, i} = f_{i\sigma}^+ f_{i\sigma} - \frac{1}{2}$, t_{ij} are the metal hoppings, ϵ_0 is the flat band energy, V is the Kondo hybridization between the f orbital and the c orbital directly below it, and U is the effective Hubbard interaction for the flat band. Since there is one moment per 13 metal atoms, this is a dilute Kondo lattice¹⁰. In the large U limit where charge fluctuations are frozen, the f -level can be represented as a spin $\frac{1}{2}$ exchange-coupled to the metal spins via a Schrieffer-Wolf transformation, giving rise to the Kondo lattice model

$$H = \sum_{i,j \in H, \sigma} t_{ij} c_{i\sigma}^+ c_{j\sigma} + \sum_{i \in T, \sigma} J_K \vec{S}_{f, i} \cdot \vec{S}_{c, i},$$

where $J_K = 8 V^2/U$ is the Kondo coupling, $\vec{S}_{f, i}$ is the effective moment at SoD site i , and $S_{c, i} = \frac{1}{2} c_i^+ \vec{\sigma} c_i$ is the metal spin directly below the SoD center. The predictions of this model are well known: a Kondo resonance emerges at each impurity at $T_K = W e^{-\frac{1}{\rho J_K}}$, where ρ is the Fermi level DOS and W the metal bandwidth. As temperature is further lowered, two ground states can be realized: RKKY magnetic order occurs at low values of J_K , while Kondo paramagnetism occurs at high J_K , with a quantum critical point separating them at $J_K \rho \sim 1$ (refs. 1,11,12). Knowledge of the dimensionless parameter $J_K \rho$ is therefore of key importance to interpret our results.

To estimate the values of the model parameters, we performed *ab initio* calculations of the band structures for the 1H-, 1T- and 1H/1T-TaSe₂ structures (see SM). The 1H polytype presents a single half-filled d -orbital band at the Fermi level, with a bandwidth of $W = 1.2$ eV and a Fermi level

DOS of $\rho = 2.5 \text{ eV}^{-1}$ (we neglected the known 3×3 reconstruction of this band for simplicity, see SM). The 1T polytype displays the $\sqrt{13} \times \sqrt{13}$ reconstruction with a half-filled flat-band of width 25 meV lying within the CDW gap of 0.55 eV and with its real space spectral weight concentrated in the central atom of the SoD pattern, all consistent with previous reports¹³⁻¹⁵. Our calculation of the 1T/1H heterostructure reveals a set of bands that correspond to those of 1T and 1H sublayers, with a weak hybridization and weak charge transfer from the T to the H layer. This band structure can be fitted with the periodic Anderson model discussed above at $U = 0$ to obtain the metal dispersion and Kondo hybridization V . To do so, we first fitted the uncoupled 1H metal band, and then coupled it to a single flat band representing the 1T layer with constant hybridization V which was left as a fitting parameter (see SM for details). Good agreement with the *ab-initio* bands was obtained for V in the range $V = 15\text{-}20$ meV. With the value of U obtained experimentally $U = 208 \pm 4$ meV, which is consistent with *ab initio* estimates for the effective Hubbard U of the flat band in other 1T TMDs^{16,17}, we finally obtain $J_K = 8 V^2/U = 8\text{-}15$ meV. Taken at face value, the product $J_K \rho = 0.037$ then clearly indicates we should be deep into the magnetic side of the Doniach diagram. An order of magnitude estimate for J_K can also be obtained from the measured Kondo temperatures^{4,5} $T_K = W e^{-\frac{1}{\rho J_K}}$, which yields somewhat larger values $J_K \rho \sim 0.1$, but still in the magnetic side.

Our Kondo lattice model can next be used to rationalize the magnetic field dependence of the split Kondo peak, which we will argue is also consistent with magnetic order, but not with a Kondo insulator. The essential low-energy features in tunneling to the localized magnetic orbitals are known from mean-field^{18,19} and quantum Monte Carlo (QMC) studies of the Kondo lattice^{11,12,20,21}. In the mean-field picture, for energies much lower than U , the localized spin is represented by an auxiliary low-energy fermion \tilde{f} as $\vec{S}_f = \tilde{f}^+ \vec{\sigma} \tilde{f}$, and the Kondo exchange is decoupled as $J_K \vec{S}_c \cdot \vec{S}_f \rightarrow J_K [\tilde{V}(\tilde{f}^+ c + c^+ \tilde{f}) + \vec{S}_f \cdot \langle \vec{S}_c \rangle + \vec{S}_c \cdot \langle \vec{S}_f \rangle]$ with $\tilde{V} = \langle c^+ \tilde{f} \rangle$ the renormalized Kondo hybridization. This auxiliary fermion band is pinned to E_F and represents the low-energy Kondo peak, which emerges at $T \sim T_K$. Further lowering the temperature leads to a splitting of the Kondo peak of different origins, due to the different finite order parameters $\tilde{V}, \langle \vec{S}_c \rangle, \langle \vec{S}_f \rangle$. When $J_K > J_C$ this splitting originates from the hybridization \tilde{V} between the auxiliary fermion band and the metal and leads to a paramagnetic Kondo insulator. If $J_K < J_C$ the splitting rather originates from ferromagnetic (FM) or antiferromagnetic (AFM) order in $\langle \vec{S}_c \rangle$ ^{22,23}. A splitting of the Kondo peak is therefore not sufficient to make a claim about either ground state.

The Zeeman field dependence of the split peak is however very different in each case. In the Kondo insulator, the mean field bands are spin-degenerate, and the Zeeman field shifts the spin up

and down bands rigidly in opposite directions^{24,25} (see Fig. 1b). This gives rise to four peaks and an eventual closing of the gap²⁶. Our resolution clearly allows us to discard this scenario. In the magnetic phase, the main features in the \tilde{f} -fermion spectrum derive from the interplay between the exchange field derived from the metal magnetization $\langle \vec{S}_c \rangle$ and the Zeeman coupling

$$H_{\tilde{f}} = J_K \frac{1}{2} \tilde{f}^+ \vec{\sigma} \tilde{f} \langle \vec{S}_c \rangle - \frac{1}{2} \mu_B g \vec{B} \tilde{f}^+ \vec{\sigma} \tilde{f},$$

where μ_B is the Bohr magneton and $g = 4.3$ is the measured g-factor. The gap of the \tilde{f} -fermion is obtained as $\Delta = |J_K \langle \vec{S}_c \rangle - \mu_B g \vec{B}|$, from which several general statements can be made, even without knowing the full B_z -dependent mean-field solution for $\tilde{V}, \langle \vec{S}_c \rangle, \langle \vec{S}_f \rangle$. First, the Zeeman coupling polarizes $\langle \vec{S}_f \rangle$, which leads to $\langle \vec{S}_c \rangle$ of opposite sign due to the AFM Kondo coupling. If $\vec{S}_c \parallel \vec{B}$, then the gap depends on B_z as $\Delta = |J_K S_c(B_z) - \mu_B g B_z|$, (with $S_c(B_z) < 0$ for $B_z > 0$). Regardless of the form of $S_c(B_z)$, it is clear that Δ will not be symmetric in B_z and will be zero when the Zeeman field flips the spin polarization, represented in Fig. 6a for the simplest case of constant S_c . However, if $\vec{S}_c \perp \vec{B}$, $\Delta = \sqrt{(J_K^2 S_c^2(B_z) + \mu_B^2 g^2 B_z^2)}$, and Δ grows symmetrically with B_z (Fig. 6b, again for constant S_c). Our observations are therefore consistent with in-plane magnetic order (FM or AFM since these cannot be distinguished without dispersion for the \tilde{f} -fermion).

The non-linear low-field behavior of the gap can also be understood assuming a smooth canting function $\langle \vec{S}_c \rangle(B_z) = (\cos(b) S_c^0, 0, \sin(b) S_c^{max})$ with $b = \frac{\pi}{2} \frac{B}{B_c}$, which interpolates between in-plane and out-of-plane order that saturates at $B_c = 0.5$ T. S_c^0 can be obtained from the measured $\Delta = 1.2$ meV at zero field and $J_K = 15$ meV as $S_c^0 \sim 0.066$, while S_c^{max} is the intercept of the linear fit with $B = 0$ T (see Fig. 5b), which is on average $\Delta + S = 1.35$ meV and gives the value of $S_c^{max} = 0.077$. With these parameters, we obtain $\Delta(B_z)$ shown in Fig 6c for different values of S_c^0 . The qualitative non-linear behavior of the experiment is well reproduced with this model when $S_c^0 < S_c^{max}$, with a faster growth below B_c and a slower one above it. In some instances, we have also observed the opposite behavior (see SM), which is obtained for $S_c^0 > S_c^{max}$ in the model. The non-linear behavior is therefore supportive of a Zeeman-induced transition from in-plane to out-of-plane order.

Lastly, we can gain understanding of the mechanism selecting the in-plane order by considering the actual magnetic susceptibility of itinerant electrons of the 1H layer. Isolated 1H-TMD metals are predicted to be close to a magnetic instability with anomalously large spin susceptibilities. Calculations for the isoelectronic NbSe₂ reveal two leading instabilities, an in-plane AFM (or spin-

spiral) with period 4-5 lattice constants^{10,27,28}, and a subleading fully ferromagnetic state^{28,29}. The periodicity of the in-plane AFM state is very close to that of the SoD periodicity, which makes the emergence of AFM order natural. Nevertheless, the subleading ferromagnetic instability makes the moments relatively soft for tilting out of the plane. Our experiment therefore reveals an interesting connection between the magnetic states of the 1T/1H Kondo lattice and the purported instabilities of the isolated H layer.

Our work demonstrates that the coherence regime in the artificial 2D Kondo lattice realized in 1T/1H TMD heterobilayers can be accessed experimentally, placing the 1T/1H-TaSe₂ system safely on the magnetic side of the Doniach phase diagram. The realization of a coherent 2D Kondo lattice with magnetic order enables a model platform where sought-after Kondo phenomenology can be studied with unprecedented resolution and tunability. Several avenues are now opened to fully characterize and tune this versatile Kondo platform, for example by using probes with magnetic sensitivity such as spin susceptibility or spin-resolved STS, which can offer detailed information about the exact magnetic ground state. Beyond their characterization, gated devices would allow to approach the critical point, offering an unprecedented window to access the quantum criticality regime, and potentially to induce unconventional superconductivity^{30,31}.

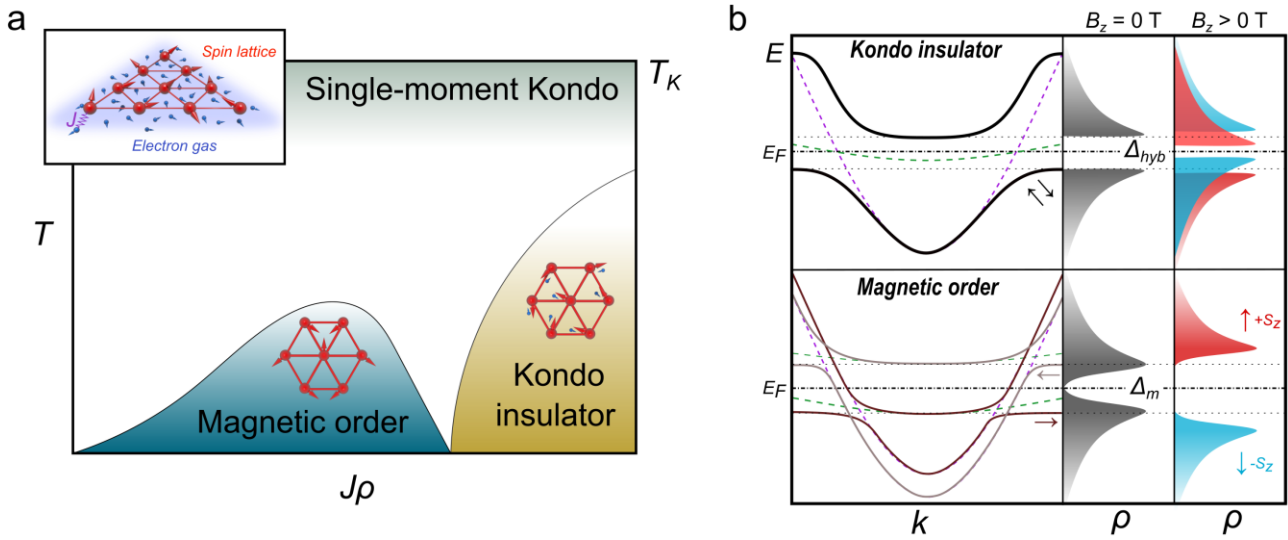


Figure 1 | Ground state of a Kondo lattice. **a**, Doniach phase diagram of a Kondo lattice showing its two possible electronic ground states at low temperatures, the magnetic order and Kondo insulator. The inset shows a representation of the spin lattice (red) and the itinerant electron gas from the metal (blue). J is the local exchange coupling between the localized magnetic moment and the conduction electrons. **b**, Schematic band structures and spin-resolved (z component) density of states (ρ) of the two ground states. In a Kondo insulator (upper panel), the conduction band (purple curve) and the localized states (green curve) hybridize to form two spin-degenerate electronic bands (black curves) separated by a gap (Δ_{hyb}). If the Kondo lattice develops magnetic order (lower panel), spin-polarized electronic bands emerge around E_F , which leads to two peaks in ρ separated by Δ_m . In the presence of an external magnetic field in the out-of-plane direction, however, ρ develops differently and both ground states can be distinguished.

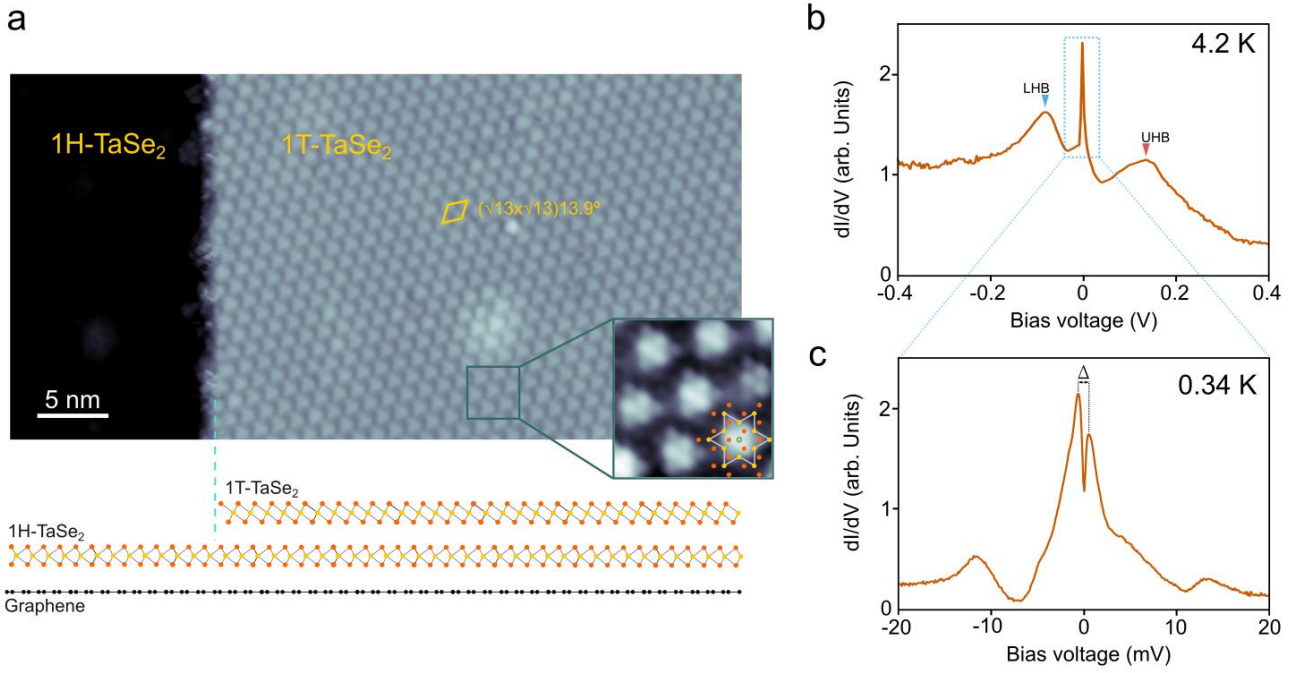


Figure 2 | Atomic and electronic structure of the 1T-TaSe₂/1H-TaSe₂ heterobilayer. **a**, Large-scale STM image of a monolayer of 1T-TaSe₂ on monolayer 1H-TaSe₂ grown on BLG/SiC(0001) ($V_s = -2$ V, $I = 0.08$ nA, $T = 4.2$ K). Below a sketch of the vertical arrangement of the atomic layer is shown. Se, Ta and C atoms are displayed in orange, yellow and black, respectively. The inset shows a high-resolution STM image of the CDW supercell, where a sketch of the SoD is overlaid ($V_s = -2.5$ mV, $I = 2$ nA, $T = 0.34$ K). **b**, Typical dI/dV spectrum taken on the 1T/1H heterostructure at 4.2 K ($V_{a.c.} = 1$ mV). The position of the lower (upper) Hubbard bands are indicated. **c**, Low-bias dI/dV spectrum acquired on the 1T/1H heterostructure at our base temperature of 0.34 K showing the emergence of two peaks ($V_{a.c.} = 50$ μ V, $B = 0$ T). The energy separation (Δ) between the peaks maxima is indicated.

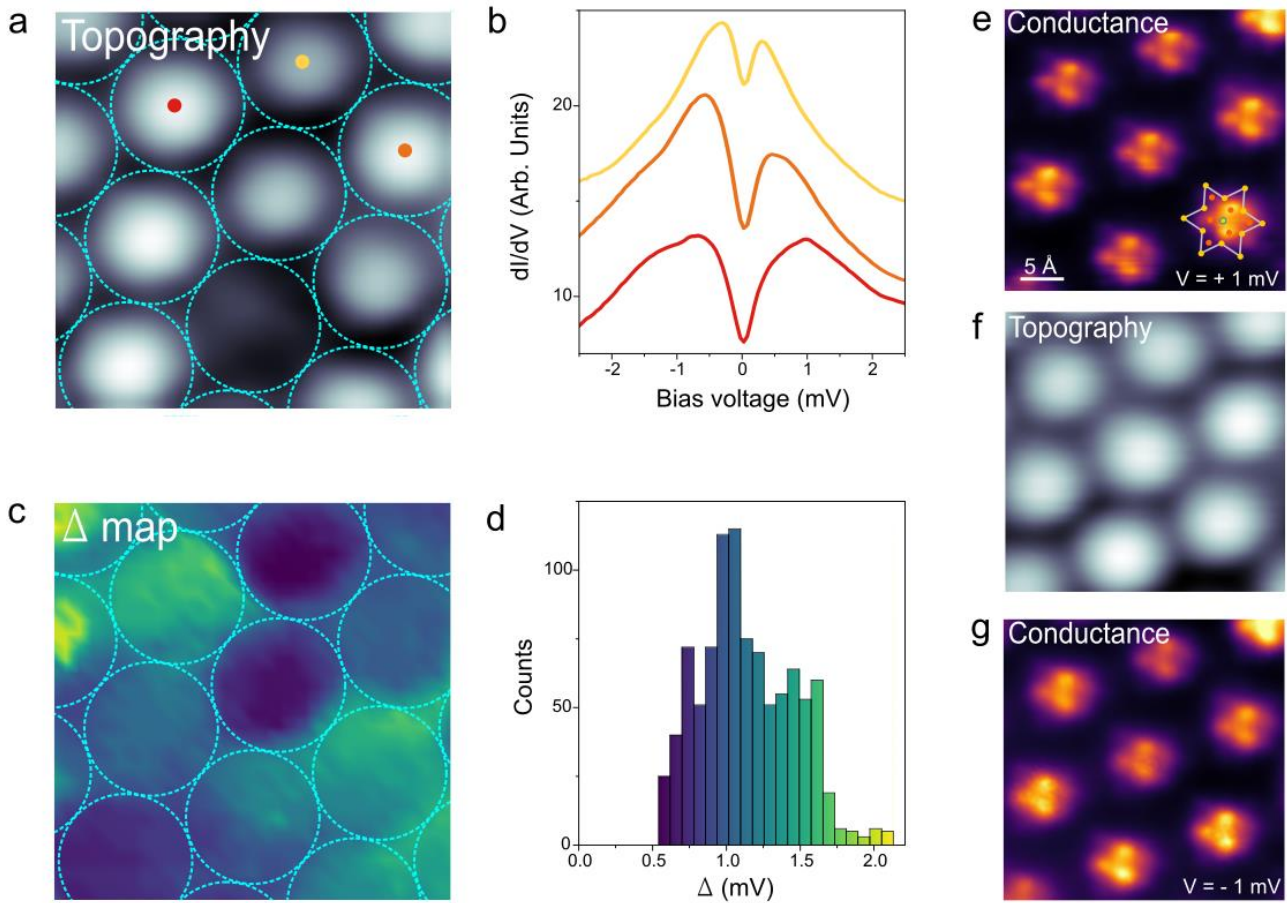


Figure 3 | Spatial mapping of the low-energy electronic structure. **a**, STM topography of the 1T/1H heterostructure ($V_s = 4$ mV, $I = 1.5$ nA, $T = 0.34$ K, 3.3×3.3 nm²). The blue circles represent the boundaries of the Star-of-David clusters. **b**, dI/dV spectra taken at the center of the three neighboring clusters indicated dots in **a** ($V_{a.c.} = 40$ μ V, $B = 0$ T). **c**, Spatially resolved map of Δ (separation of peaks) taken in the region shown in **a**. The map is extracted from a 40×40 dI/dV grid acquired at 0.34 K ($V_{a.c.} = 40$ μ V, $B = 0$ T). The color scale of the Δ map is shown in the histogram in **d**. **e**, Conductance map (constant height) acquired at $V_s = +1$ mV. The atomic position of the SoD cluster is indicated. **f**, Topograph of the region where the conductance maps were taken ($V_s = -5$ mV, $I = 0.18$ nA,). **g**, Conductance map at the opposite polarity ($V_s = -1$ mV) in the same region (for both conductance maps: $V_{a.c.} = 20$ μ V, $B = 0$ T, $T = 0.34$ K).

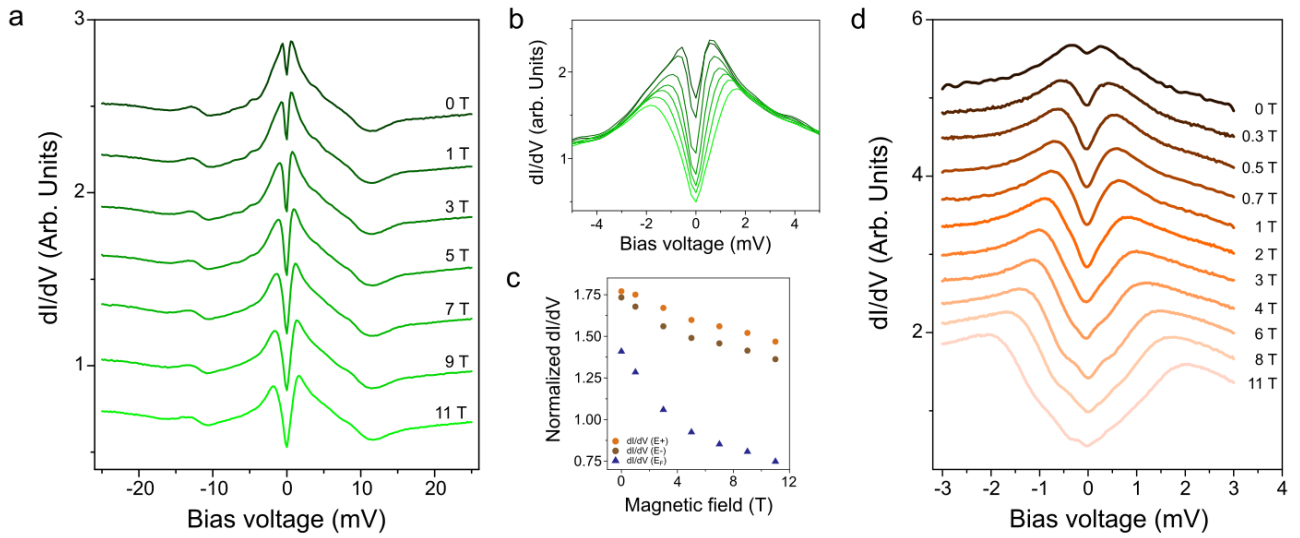


Figure 4 | Magnetic field dependence of the low-energy electronic structure. a, Set of dI/dV spectra taken consecutively at $T = 0.34$ K as the perpendicular magnetic field is varied in the 0-11 T range ($V_{a.c.} = 50 \mu\text{V}$). **b,** Zoom-in of the set shown in **a**. The curves are normalized to the set-point voltage ($V_b = +25$ mV). **c,** Differential conductance values measured at the peaks maxima (E^+ (orange circles) and E^- (brown circles)) and E_F (blue triangles) in the dI/dV spectra shown in **a**. **d,** High-resolution series of dI/dV spectra taken consecutively at $T = 0.34$ K in the vicinity of E_F ($V_{a.c.} = 30 \mu\text{V}$).

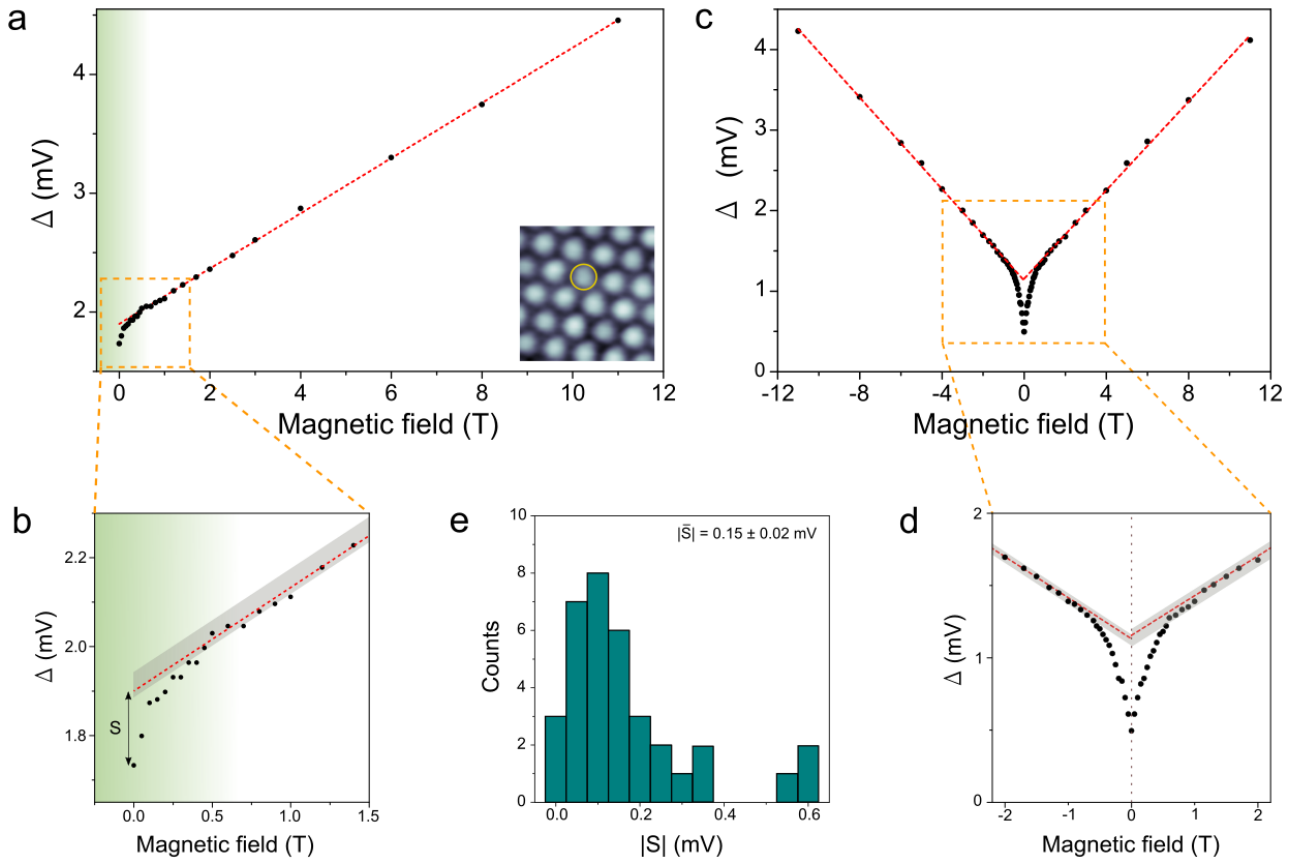


Figure 5 | Non-linear behavior of Δ with the magnetic field. **a**, Plot of Δ as a function of B_z for a series of dI/dV spectra taken consecutively in the SoD cluster shown in the inset. The red dashed line is the linear fit realized in the $1\text{T} < B_z < 11\text{T}$. The green shadow indicates the range of B_z where Δ deviates from a linear relation. **b**, Zoom-in of the boxed region in **a**. The grey region indicates the uncertainty band of Δ in the linear region (see SM). **c**, Plot of Δ as a function of B_z for a series of dI/dV spectra taken consecutively in the range $\pm 11\text{T}$. The red dashed lines are the linear fits. **d**, Zoom-in of the boxed region in **c**. **e**, Histogram showing the occurrence of $|S|$ for the different SoD clusters explored within $0\text{T} < B_z < 11\text{T}$.

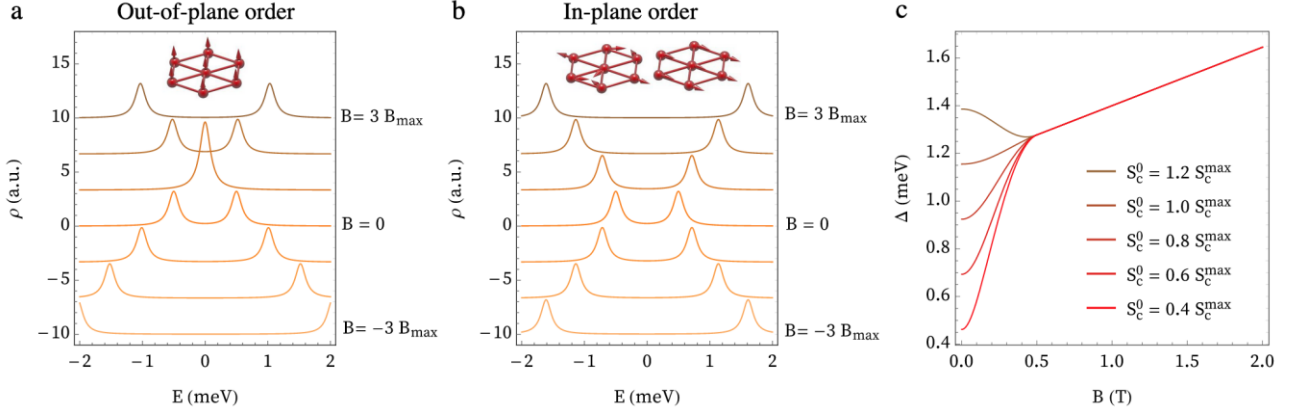


Figure 6 | Splitting patterns from mean-field \tilde{f} -fermion description. **a**, Schematic dependence of the spectral function with out-of-plane ferromagnetic order, for different values of the field in integer multiples of $B_{max} = J_K S_c^{max} / g\mu_B$. At low fields, the peak splitting decreases when the field polarity is opposite to the narrow band magnetization, but it increases when they are aligned. **b**, Spectral function with in-plane order. The peaks split symmetrically with magnetic field polarity. **c**, Non-linear behavior of the gap for the in-plane case due to the reorientation and increased magnitude of the magnetic moment as the field is applied, for $S_c^{max} = 0.077$, $B_c = 0.5$ T and different values of the initial moment S_c^0 .

References

1. Doniach, S. The Kondo lattice and weak antiferromagnetism. *Phys. B+C* **91**, 231–234 (1977).
2. Ernst, S. *et al.* Emerging local Kondo screening and spatial coherence in the heavy-fermion metal YbRh₂Si₂. *Nature* **474**, 362–366 (2011).
3. Aynajian, P. *et al.* Visualizing heavy fermions emerging in a quantum critical Kondo lattice. *Nature* **486**, 201–206 (2012).
4. Ruan, W. *et al.* Evidence for quantum spin liquid behaviour in single-layer 1T-TaSe₂ from scanning tunnelling microscopy. *Nat. Phys.* **17**, 1154–1161 (2021).
5. Vaño, V. *et al.* Artificial heavy fermions in a van der Waals heterostructure. *Nature* **599**, 582–586 (2021).
6. Liu, M. *et al.* Monolayer 1T-NbSe₂ as a 2D-correlated magnetic insulator. *Sci. Adv.* **7**, eabi6339 (2021).
7. Shen, S. *et al.* Inducing and tuning Kondo screening in a narrow-electronic-band system. *Nat. Commun.* **13**, 1–7 (2022).
8. Wang, Z. *et al.* Surface-Limited Superconducting Phase Transition on 1T-TaS₂. *ACS Nano* **12**, 12619–12628 (2018).
9. Ayani, C. G. *et al.* Two-dimensional Kondo lattice in a TaS₂ van der Waals heterostructure. (2022) doi:10.48550/arxiv.2205.11383.
10. Costa, A. T., Costa, M. & Fernández-Rossier, J. Ising paramagnons. *arXiv* 2110.09809 (2021).
11. Vekić, M., Cannon, J. W., Scalapino, D. J., Scalettar, R. T. & Sugar, R. L. Competition between Antiferromagnetic Order and Spin-Liquid Behavior in the Two-Dimensional Periodic Anderson Model at Half Filling. *Phys. Rev. Lett.* **74**, 2367 (1995).
12. Assaad, F. F. Quantum Monte Carlo Simulations of the Half-Filled Two-Dimensional Kondo Lattice Model. *Phys. Rev. Lett.* **83**, 796 (1999).
13. Zhang, K., Si, C., Lian, C. S., Zhou, J. & Sun, Z. Mottness collapse in monolayer 1T-TaSe₂ with persisting charge density wave order. *J. Mater. Chem. C* **8**, 9742–9747 (2020).
14. Jiang, T. *et al.* Two-dimensional charge density waves in TaX₂ (X= S, Se, Te) from first principles. *Phys. Rev. B* **104**, 075147 (2021).
15. Chen, Y. *et al.* Strong correlations and orbital texture in single-layer 1T-TaSe₂. *Nat. Phys.* **16**, 218 (2020).
16. Kamil, E. *et al.* Electronic structure of single layer 1T-NbSe₂: interplay of lattice distortions, non-local exchange, and Mott–Hubbard correlations. *J. Phys. Condens. Matter* **30**, 325601 (2018).
17. Pasquier, D. & Yazyev, O. V. Ab initio theory of magnetism in two-dimensional 1T-TaS₂. *Phys. Rev. B* **105**, L081106 (2022).
18. Dorin, V. & Schlottmann, P. Magnetic instabilities in Kondo insulators. *Phys. Rev. B* **46**, 10800 (1992).
19. Zhang, G. M. & Yu, L. Kondo singlet state coexisting with antiferromagnetic long-range order: A possible ground state for Kondo insulators. *Phys. Rev. B* **62**, 76 (2000).
20. Capponi, S. & Assaad, F. F. Spin and charge dynamics of the ferromagnetic and antiferromagnetic two-dimensional half-filled Kondo lattice model. *Phys. Rev. B* **63**, 155114 (2001).

21. Danu, B., Liu, Z., Assaad, F. F. & Raczkowski, M. Zooming in on heavy fermions in Kondo lattice models. *Phys. Rev. B* **104**, 155128 (2021).
22. Aulbach, M. W., Assaad, F. F. & Potthoff, M. Dynamical mean-field study of partial Kondo screening in the periodic Anderson model on the triangular lattice. *Phys. Rev. B* **92**, 235131 (2015).
23. Keßler, M. & Eder, R. Magnetic phases of the triangular Kondo lattice. *Phys. Rev. B* **102**, 235125 (2020).
24. Saso, T. Self-Consistent Perturbational Study of Insulator-to-Metal Transition in Kondo Insulators due to Strong Magnetic Field. *J. Phys. Soc. Japan* **66**, 1175–1179 (1997).
25. Beach, K. S. D. & Assaad, F. F. Coherence and metamagnetism in the two-dimensional Kondo lattice model. *Phys. Rev. B* **77**, 205123 (2008).
26. Jaime, M. *et al.* Closing the spin gap in the Kondo insulator Ce₃Bi₄Pt₃ at high magnetic fields. *Nature* **405**, 160–163 (2000).
27. Zheng, F., Zhou, Z., Liu, X. & Feng, J. First-principles study of charge and magnetic ordering in monolayer NbSe₂. *Phys. Rev. B* **97**, 081101(R) (2018).
28. Wickramaratne, D., Khmelevskiy, S., Agterberg, D. F. & Mazin, I. I. Ising Superconductivity and Magnetism in NbSe₂. *Phys. Rev. X* **10**, 041003 (2020).
29. Divilov, S. *et al.* Magnetic correlations in single-layer NbSe₂. *J. Phys. Condens. Matter* **33**, 295804 (2021).
30. Ribak, A. *et al.* Chiral superconductivity in the alternate stacking compound 4Hb-TaS₂. *Sci. Adv.* **6**, 9480–9507 (2020).
31. Nayak, A. K. *et al.* Evidence of topological boundary modes with topological nodal-point superconductivity. *Nat. Phys.* **17**, 1413–1419 (2021).

Acknowledgements

M.M.U. acknowledges support by the ERC Starting grant LINKSPM (Grant 758558) and by the Spanish MINECO under grant no. MAT2017-88377-C2-1-R. R.H. acknowledges support from Marie Skłodowska-Curie Individual Fellowships under HORIZON 2020 program for project MAGTMD (101033538). F. J. acknowledges funding from the Spanish MCI/AEI/FEDER (grant PGC2018-101988-B-C21) and from the Diputacion de Gipuzkoa through Gipuzkoa Next (grant 2021-CIEN-000070-01).

Author contributions

W.W. carried out the MBE growth, the morphology characterization of the samples with the help of R.H., P.D. and S.S.. W.W. measured and analyzed the STM/STS data with the help of R.H., P.D., S.S. and M.M.U.. A. M. and I. E. carried out the *ab initio* calculations. M.M.U. supervised the project. F.J. provided the theoretical support and participated in the interpretation of the experimental data. M.M.U. and F.J. wrote the paper with help from the rest of the authors. All authors contributed to the scientific discussion and manuscript revisions.

Supplementary Materials for

Magnetic order in a coherent two-dimensional Kondo lattice

Wen Wan¹, Rishav Harsh¹, Antonella Meninno^{2,3}, Paul Dreher¹, Sandra Sajan¹,

Ion Errea^{1,2,3}, Fernando de Juan^{*,1,4} and Miguel M. Ugeda^{*,1,2,4}

¹*Donostia International Physics Center (DIPC), Paseo Manuel de Lardizábal 4, 20018 San Sebastián, Spain.*

²*Centro de Física de Materiales, Paseo Manuel de Lardizábal 5, 20018 San Sebastián, Spain.*

³*Departamento de Física Aplicada, Escuela de Ingeniería de Gipuzkoa, University of the Basque Country (UPV/EHU), Plaza Europa 1, 20018 San Sebastián, Spain.*

⁴*Ikerbasque, Basque Foundation for Science, 48013 Bilbao, Spain.*

* Corresponding authors: fernando.dejuan@dipc.org and mmugeda@dipc.org

1. Growth of 1T-TaSe₂/1H-TaSe₂ heterobilayers and large-scale morphology

1T-TaSe₂/1H-TaSe₂ heterobilayers were grown on BLG/SiC (0001) substrates in a two-step process in our home-made ultra-high vacuum molecular beam epitaxy (UHV-MBE) system under base pressure of $\sim 5.0 \times 10^{-10}$ mbar. First, uniform bilayer graphene was prepared by direct annealing 4H-SiC (0001) at a temperature around 1400°C for 35 minutes. Second, the as-grown BLG/SiC (0001) substrates were maintained around 550°C to grow monolayer 1H-TaSe₂ by co-evaporation of high-purity Ta (99.95%) and Se (99.999%) with a flux ratio (Ta:Se) of $\sim 1:30$. The growth rate for TaSe₂ was 2.5 hours/monolayer. Third, the temperature of the substrate was then increased to 640°C while keeping evaporation parameters unchanged to obtain 1T-TaSe₂. After the growth, the samples were kept annealed in Se environment for 2 minutes, and then immediately cooled down to room temperature. The growth was monitored in-situ by reflection high-energy electron diffraction (RHEED). A ~ 10 nm-thick Se layer was deposited on the prepared sample before taking it out of UHV conditions for further ex-situ UHV-STM measurements. The Se capping layer was subsequently removed in the UHV-STM by annealing at ~ 300 °C for 40 minutes.

After this process, the typical morphology of our samples, as seen in the STM is shown in Fig. S1. Large islands (~ 200 nm in diameter) of single-layer 1H-TaSe₂ are grown on BLG, often decorated by second upper layers (~ 60 nm). Most of these upper layers belong to the 1T polytype, thus forming the 1T-TaSe₂/1H-TaSe₂ heterobilayer that has been in studied here.

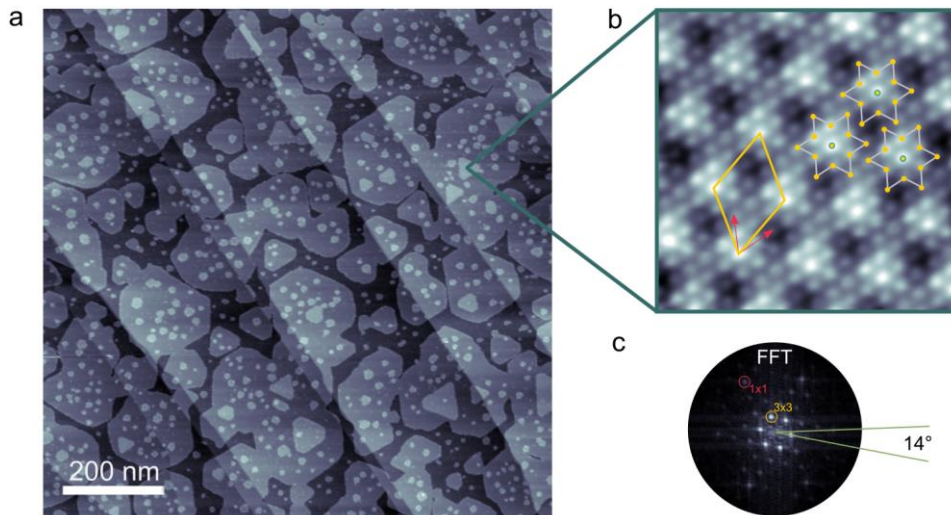


Fig. S1. Morphology of the 1T-TaSe₂/1H-TaSe₂ heterobilayer. **a**, Large-scale STM image of TaSe₂ on BLG/SiC(0001) ($V_s = 1.8$ V, $I = 0.02$ nA, $T = 4.2$ K). **b**, Atomically resolved STM image taken on 1T-TaSe₂/1H-TaSe₂ ($V_s = -0.25$ V, $I = 0.1$ nA, $T = 0.34$ K). Three Star-of-David clusters are overlaid. The yellow rhombus shows the CDW supercell and the red arrows indicate the directions of the atomic registry. **c**, Fast Fourier transform (FFT) of the STM image in **b**, which shows the $\sim 14^\circ$ rotational misalignment between the CDW and the atomic lattice.

2. STM/STS measurements and tip calibration

STM/STS data were acquired in a commercial UHV-STM system equipped with perpendicular magnetic fields up to 11 T (Unisoku, USM-1300). The measurements were carried out at temperatures between 340 mK and 4.2 K with Pt/Ir tips. To avoid tip artifacts in our STS measurements, the STM tips were calibrated using a Cu(111) surface as reference. We also performed careful inspection of the DOS around E_F to avoid the use of functionalized tips showing strong variations in the DOS. The typical lock-in a.c. modulation parameters for low- and large-bias STS were 20-50 μV and $\sim 1\text{-}2$ mV at $f = 833$ Hz, respectively. We used Pt/Ir tips for the STM/STS experiments. STM/STS data were analyzed and rendered using WSxM software¹.

3. Temperature-dependent low-energy electronic structure

Low-bias STS measurements at 4.2 K display a single peak centered around E_F , which turns into a double-peak feature at $T = 0.34$ K. We have probed the evolution of the low-energy electronic structure in the range 0.34 K – 4.5 K. Figure S2a shows a series of dI/dV spectra taken on a Star-of-David that showing the two-peak feature at 0.34 K. The position of the peaks is temperature independent and the only visible effect is the gradual filling of the conductance at E_F , which is attributed to thermal broadening. Δ remains nearly constant with T (fig. S2b) and cannot be further identified beyond 4-5 K due to thermal broadening. In conclusion, these results show that the emergence of two peaks as T lowers is not gradual (T -dependent process) but rather due to an increase of STS resolution. It is therefore plausible that the emergence of coherence of the magnetic moments occur at higher temperatures.

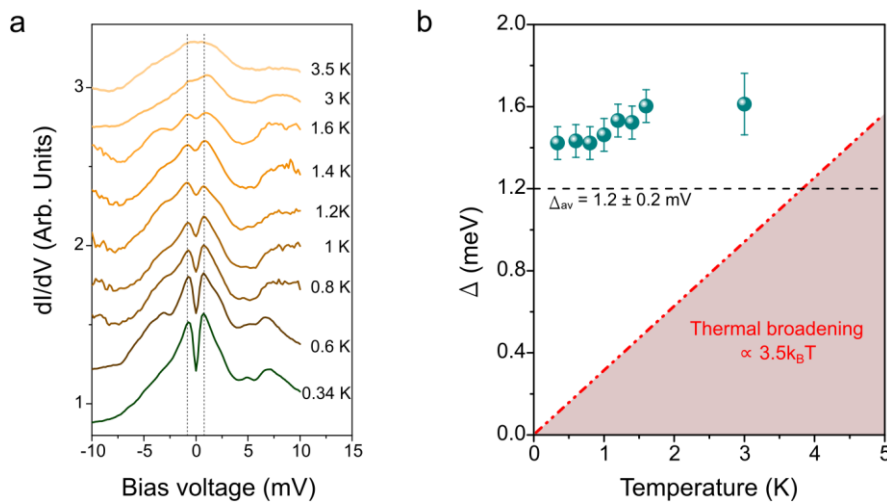


Fig. S2. Temperature dependence of the low-energy electronic structure. **a**, Series of low-bias dI/dV spectra taken in the 0.34 – 3.5 K range ($V_{a.c.} = 30$ μV). **b**, Δ vs. T for the dI/dV set in **a**. The shaded area indicates the region where Δ cannot be resolved via STS due to thermal broadening.

4. Lower and upper Hubbard band in 1T-TaSe₂ on 1H-TaSe₂

The realization of the Kondo effect (either for a single impurity or for a Kondo lattice) implies the existence of two localized resonances in tunneling above and below the Fermi level, which correspond to the localized level with energy ϵ_f occupied by a single electron, and the doubly occupied level which has energy $\epsilon_f + U$ due to the local Coulomb (Hubbard) repulsion, and which are usually referred to as lower and upper Hubbard bands. In our STS experiments, we observe two peaks at $V_{\text{LHB}} = -77 \pm 4$ mV and $V_{\text{UHB}} = 131 \pm 4$ mV, which we identify as the LHB and UHB, respectively (Fig. 2 of the main manuscript). This yields a measurement of $U = 208 \pm 4$ meV for the effective Hubbard repulsion of the localized Wannier orbital at the Star-of-David center, which gives rise to the flat band. This identification is mainly based on the following arguments. First, the experimental U found here for 1T-TaSe₂ is in good agreement with those predicted for similar 1T-TMD monolayers. In particular, previous *ab initio* calculations estimate effective Hubbard U values of 0.3 eV (ref.2) and 0.33 eV (ref.3) in 1T-NbSe₂ and 1T-TaS₂, respectively. Furthermore, another piece of evidence is provided by the spatial extension associated with these two peaks. Figure S3 shows two conductance maps taken at the maxima of the peaks, i.e. -80 mV and +130 mV for the LHB and UHB, respectively. In both cases the intensity is well localized around the Star-of-David cluster and has its maxima at its center, coincident with the expected spatial localization of the flat band in the CDW state. Lastly, the identical spatial extension associated with these two peaks suggests a common orbital origin.

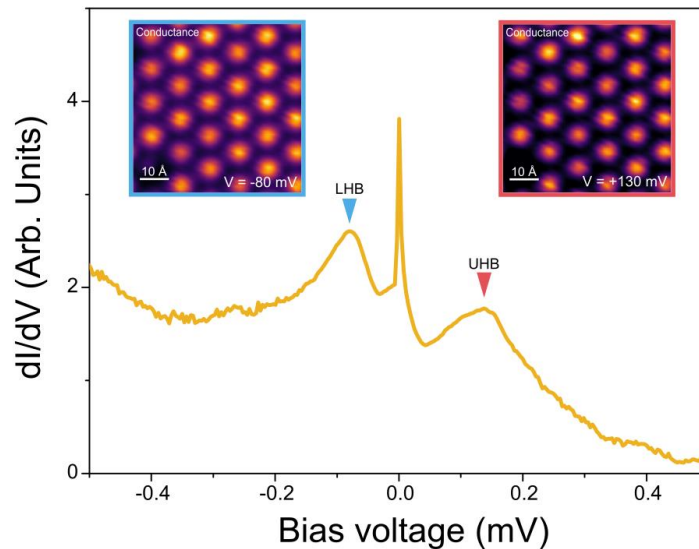


Fig. S3. Spatial extension of the LHB and UHB. Typical dI/dV curve acquired on the 1T/1H-TaSe₂ heterobilayer where the energy location of the LHB and UHB is indicated ($T = 0.34$ K). The two insets show two conductance maps acquired at the LHB and UHB energy maxima (Conductance maps: $V_{a.c.} = 40$ μ V, $B = 0$ T, $T = 0.34$ K).

5. The 1H-TaSe₂/BLG substrate

In our experiments, the array of effective magnetic moments in the 1T-TaSe₂ monolayer rests on a single layer of 1H-TaSe₂, a metal with structural and electronic properties that are reviewed in this section. The H polytype of TaSe₂ in the single-layer form is a metal with CDW order⁴ below 130 K. At 4.2 K, the CDW develops a commensurate 3 × 3 periodicity that can be easily visualized in STM images (fig. S4a). STS measurements show a metallic character of this 2D material although with a partial gap feature of width ≈10 mV centered around E_F, as seen in the dI/dV spectra shown in figs. S4b-c. This gap feature has been previously observed in 1H-TaSe₂ on two different substrates, BLG and 1T-TaSe₂, and identified as the CDW gap⁴ and, more recently, as a heavy-fermion gap⁵.

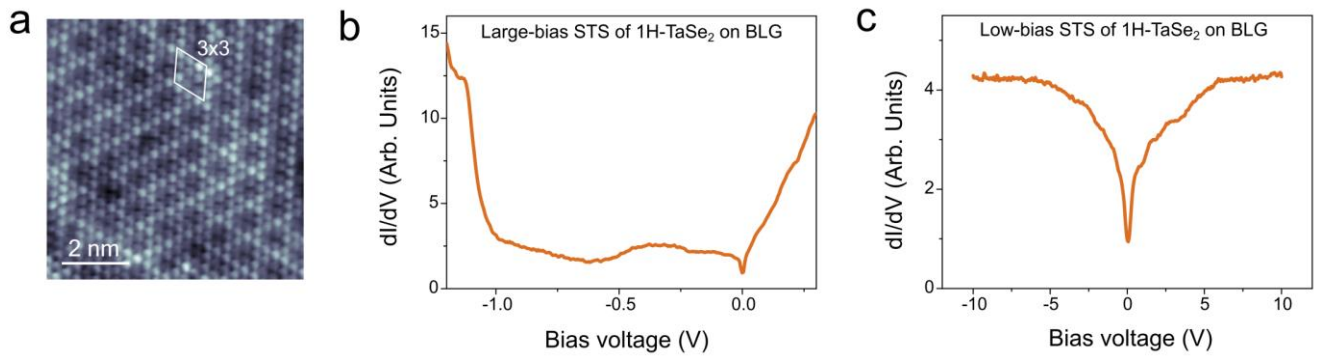


Fig. S4. Electronic structure of the 1H-TaSe₂ substrate. **a**, Atomically resolved STM image of single-layer 1H-TaSe₂ with the 3x3 CDW superlattice indicated. Large-bias (**b**) and low-bias (**c**) dI/dV spectra taken on 1H-TaSe₂ on BLG at T = 0.34 K.

6. Uncertainty band of Δ

The deviation from the linear behavior of the separation Δ between the two peaks found around E_F was found to be $\bar{\Delta} = 0.15$ mV, as shown in the main manuscript (fig.5e). This is a relatively small energy difference that, however, is larger than the uncertainty threshold imposed by our experimental noise level. In this section, we describe the procedure followed to define this confidence threshold for each B-dependent series of dI/dV spectra.

In order to estimate the confidence threshold and Δ for a given set of dI/dV spectra, we first realized a linear fit to the Δ values for $B \geq 1$ T, a magnetic field regime where the Zeeman term ($\Delta \propto g \cdot \mu_B \cdot B_z$) clearly dominates. In most of the cases, the correlation coefficient r was found to be $r > 0.99$, which indicates the strict linearity and low uncertainty of Δ with the B field. Figure S5 shows one example among the analyzed Δ vs. B_z plots. The uncertainty band was then defined as the region bound by two lines parallel to the fit line and pinned at the two experimental values showing the largest deviation above and below it for $B \geq 1$ T (green arrows in the example of fig. S5). This

uncertainty band and the linear fit are then extrapolated down to $B = 0$ T to quantify the deviations. The deviation from the linear behavior S is defined as $S = \Delta_{exp}(B = 0T) - \Delta_{fit}(B = 0T)$. The upper/lower boundaries of the band mark the uncertainty threshold of the measurements. Deviations smaller than the threshold were not included in the statistical analysis.

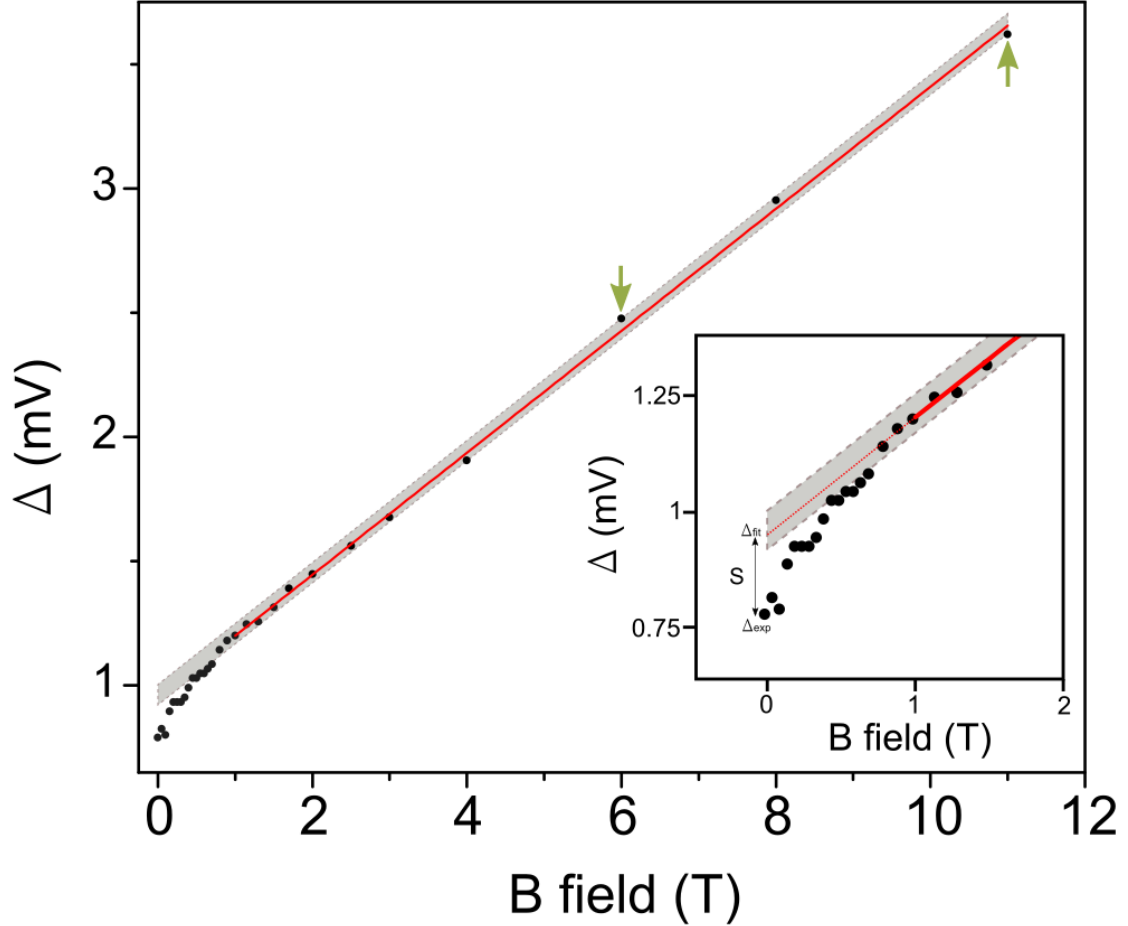


Fig. S5. Uncertainty band and non-linear behavior of Δ . Example of the analysis of the uncertainty band (grey band) from the linear fit (red line) of a set of values. The inset shows a zoom-in of the main plot in the non-linear region.

7. Measurement of the evolution of Δ with the magnetic field

In order to carry out the statistical analysis of the behavior of Δ with B_z , we measured two different samples, ten different locations (heterobilayers) and, in total, in 36 Star-of-David clusters. The B-dependent STS measurements were all acquired in bulk regions (~ 10 nm off the edges) of the 1T/1H-heterobilayer and as far as possible from defects previously identified by STM imaging at different bias voltages. At each location, the usual procedure was to measure simultaneously the B-dependence in several (2-4) Star-of-David clusters. These simultaneous STS measurements enabled to rule out instrumental artifacts related to non-linear output values at low magnetic fields as we measured distinct evolutions of Δ . Figure S6a-b shows an example of these simultaneous B-

dependence STS measurements on two neighboring clusters in the range $0 \text{ T} \leq B_z \leq 11 \text{ T}$ (only shown up to 2 T) (Fig. S6c). As seen, Δ deviates from the linear trend at low fields in both cases. However, in one case the experimental Δ evolves to larger values than Δ_{fit} (negative S) as B_z decreases while in the other case the opposite trend is observed. Our statistical analysis confirms that both trends are frequently seen although with different weight, as shown in the histogram of the occurrence of S (same as that shown in fig. 5e) taking into account its sign.

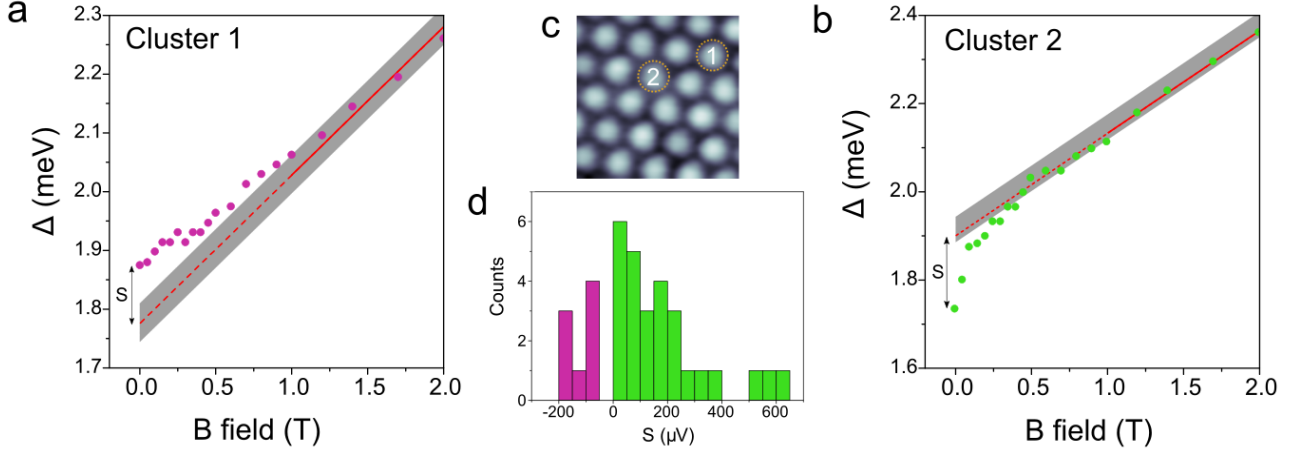


Fig. S6. Measurements of Δ . **a, b,** Plots of Δ as a function of B_z for two series of dI/dV spectra taken consecutively on the Star-of-David clusters labeled as 1 and 2 in the STM image of **c**. **d,** Histogram of the occurrence of S.

8. Band structure calculations and estimate of Kondo hybridization

We performed *ab initio* calculations using density-functional theory (DFT) within the plane-wave Quantum Espresso package^{6,7} using the Perdew-Burke-Ernzerhof (PBE)⁸ parametrization of the exchange-correlation. We have used an ultrasoft pseudopotential with 13 electrons in the valence for Ta and a norm conserving pseudopotential with 6 electrons in the valence for Se. We used a kinetic energy cutoff of 45 Ry and a charge density one of 450 Ry. The structure adopted has a lattice parameter of 3.48 Å in the unit cell of the high symmetry phase and for that phase we used a $40 \times 40 \times 1$ \mathbf{k} grid and a Methfessel-Paxton smearing of 0.005 Ry for the Brillouin zone integrals⁹. For the supercell 1T in the CDW phase, we used a denser $24 \times 24 \times 1$ \mathbf{k} grid to have a good accuracy for the flat band close to the Fermi energy. We assumed the same lattice constant for the H and the T polytypes, and for simplicity we neglect the 3×3 CDW of the H phase. The 3×3 CDW in TaSe₂ is weak and does not lead to a dramatic change in the band structure or DOS. Including it in a commensurate cell with the $\sqrt{13} \times \sqrt{13}$ CDW of the T layer would require a prohibitively large unit cell.

The band structure for the H polytype in its original unit cell is shown in Fig. S7b, showing the well-known half-filled band at the Fermi level, with bandwidth $W = 1.2$ eV. Fig S7b also shows the computed density of states, with a value at the Fermi level of $\rho = 2.5$ eV⁻¹. We have fitted this band structure with a single orbital tight binding model with hoppings up to the 10th neighbor. We then refined the fit by computing the band structure for the 1H phase in the $\sqrt{13} \times \sqrt{13}$ supercell, so that now 13 bands are fitted. This contains more information than just fitting the high symmetry paths of a single band. The final values of the hoppings in eV are given as $t_i = (0.087, 0.215, -0.028, -0.006, -0.027, 0.003, -0.006, -0.013, -0.006, 0.010)$, with a dominating 2nd neighbor hopping¹⁰, and the resulting fitted band is shown in Fig. S7b.

Next we computed the bands for the 1T polytype in the CDW state, shown in Fig. S7c. We find the well-known half-filled flat band, of width 25 meV, located inside the large CDW gap of 0.55 eV between the highest fully occupied band and the lowest empty one, in line with previous calculations of 1T-TMDs¹¹⁻¹³. The flat band is found 40 meV above the highest occupied band. The exact position of the flat band within the CDW gap is known to depend on the functional used², but most calculations for 1T-TaSe₂ agree on the flat band being isolated from other bands, as we find.

To compute the bands of the 1T/1H system, we assume a perfect lattice match of the two structures in the AA stacking¹⁴, with an interlayer distance of 6.6 Å. The resulting band structure is shown in Fig. S7d. By comparing the bands with those of the uncoupled 1T and folded 1H structures (aligning the Fermi levels of all three calculations), we observe that there is a small mixing of the bands, as we expect due to the presence of interlayer hopping. We also observe a small overall downward shift of the bands coming from the 1H structure, which implies a small charge transfer from the 1T to the 1H structure.

These findings are consistent with previous work. The 1T/1H TaSe₂ structure in the absence of the 1T CDW shows both small interlayer hopping and charge transfer from 1T to 1H^{14,15}. Charge transfer can be quantified in our calculation by computing the density of states (DOS) of all three structures: 1T, 1H, and 1T/1H. Integrating the DOS for the 1H structure in the $\sqrt{13} \times \sqrt{13}$ supercell yields a total charge of 13.03 electrons per cell, consistent with a half-filled band in the original cell with one electron per cell. Computing the projected DOS in the 1H layer for the 1T/1H structure and integrating up to the Fermi level, we find 13.35 electrons, which implies a charge transfer of 0.32 electrons per supercell from the 1T to the 1H layer, consistent with a previous estimate for TaS₂ (Ref.15).

Since we are interested in the interlayer hopping strength for the flat band near the Fermi level, we now consider a tight-binding model which contains the previously fitted 1H band structure in the $\sqrt{13} \times \sqrt{13}$ unit cell, coupled to a single completely flat band at the Fermi level with a constant interlayer hopping V (which in the Kondo problem is known as the Kondo hybridization). In addition, we allow for an on-site energy δ_H to account for the downward rigid shift as observed *ab-initio*. Direct comparison of the band structure shows the best agreement between the model and the *ab-initio* calculation for $\delta_H = -50 - 60$ meV and $V = 15-20$ meV. The bands for the highest values $\delta_H = -60$ meV, $V = 20$ meV are shown in Fig. S7e. The conclusion of this calculation, revealed by the comparison of Figs. S7d-e is that the Kondo hybridization in this problem cannot reasonably be any larger than 20 meV. Assuming the value of $U = 208$ meV extracted from the experiments, this leads to an effective Kondo coupling $J_K = 8V^2/U = 15.4$ meV.

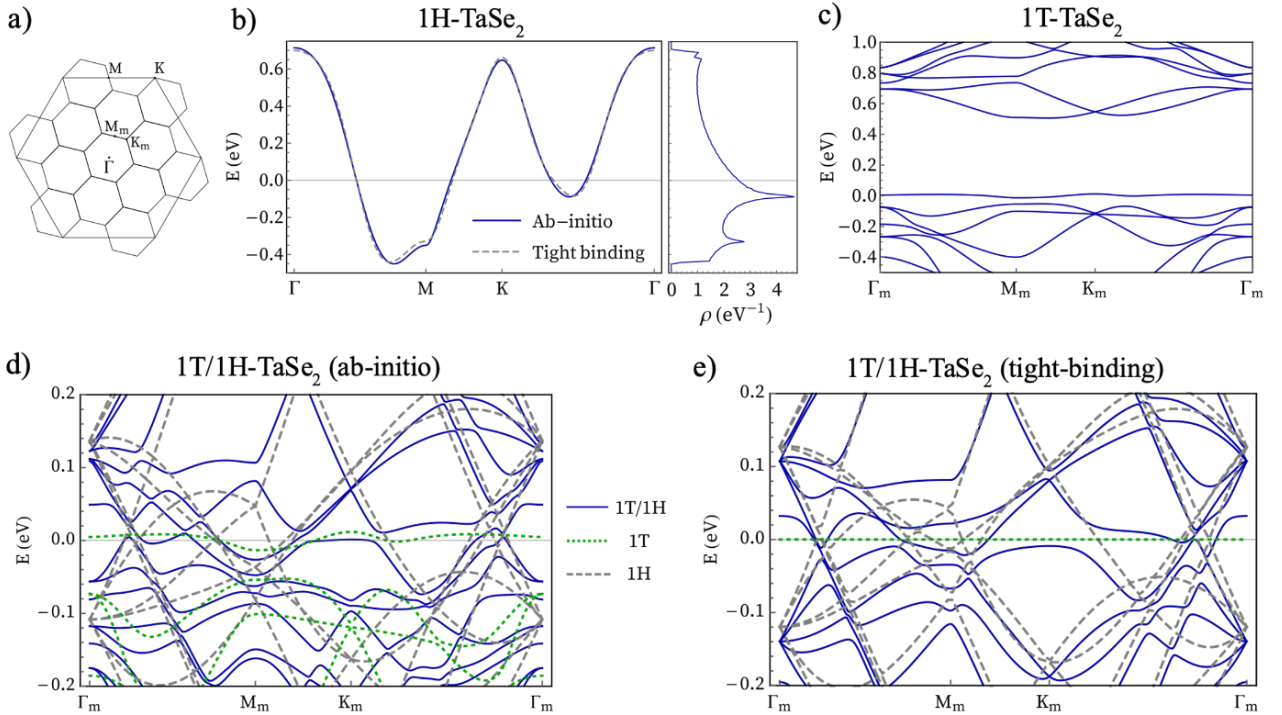


Fig. S7. Ab-initio band-structure calculations. **a**, Folding scheme showing Brillouin Zones for the 1H structure, and the 1T structure in the $\sqrt{13} \times \sqrt{13}$ CDW state. High symmetry points for the latter are labeled with a subscript m . **b**, *Ab-initio* band-structure and density of states for single layer 1H-TaSe₂. The tight binding fit discussed in the text is also shown. **c**, *Ab-initio* band-structure of single layer 1T-TaSe₂ in the CDW state. **d**, Close-up of the *ab-initio* band structure of the 1T/1H heterostructure. Bands for the isolated 1H and 1T monolayers are shown as dashed and dotted lines for comparison. **e**, Band structure of the effective tight binding model containing the fitted bands for the 1H layer and a single flat band for the 1T layer, with a Kondo hybridization between them of magnitude $V = 20$ meV. Isolated bands at $V = 0$ corresponding to isolated 1H and 1T also shown for comparison.

References

1. Horcas, I. *et al.* WSXM: A software for scanning probe microscopy and a tool for nanotechnology. *Rev. Sci. Instrum.* **78**, 013705 (2007).
2. Kamil, E. *et al.* Electronic structure of single layer 1T-NbSe₂: interplay of lattice distortions, non-local exchange, and Mott–Hubbard correlations. *J. Phys. Condens. Matter* **30**, 325601 (2018).
3. Pasquier, D. & Yazyev, O. V. Ab initio theory of magnetism in two-dimensional 1T-TaS₂. *Phys. Rev. B* **105**, L081106 (2022).
4. Ryu, H. *et al.* Persistent Charge-Density-Wave Order in Single-Layer TaSe₂. *Nano Lett.* **18**, 689–694 (2018).
5. Vaño, V. *et al.* Artificial heavy fermions in a van der Waals heterostructure. *Nature* **599**, 582–586 (2021).
6. Giannozzi, P. *et al.* QUANTUM ESPRESSO: a modular and open-source software project for quantum simulations of materials. *J. Phys. Condens. Matter* **21**, 395502 (2009).
7. Giannozzi, P. *et al.* Advanced capabilities for materials modelling with Quantum ESPRESSO. *J. Phys. Condens. Matter* **29**, 465901 (2017).
8. Perdew, J. P., Ernzerhof, M. & Burke, K. Generalized gradient approximation made simple. *Phys. Rev. Lett.* **77**, 3865–3868 (1996).
9. Methfessel, M. & Paxton, A. T. High-precision sampling for Brillouin-zone integration in metals. *Phys. Rev. B* **40**, 3616 (1989).
10. Barnett, R. L., Polkovnikov, A., Demler, E., Yin, W. G. & Ku, W. Coexistence of gapless excitations and commensurate charge-density wave in the 2H transition metal dichalcogenides. *Phys. Rev. Lett.* **96**, 026406 (2006).
11. Zhang, K., Si, C., Lian, C. S., Zhou, J. & Sun, Z. Mottness collapse in monolayer 1T-TaSe₂ with persisting charge density wave order. *J. Mater. Chem. C* **8**, 9742–9747 (2020).
12. Jiang, T. *et al.* Two-dimensional charge density waves in TaX₂ (X= S, Se, Te) from first principles. *Phys. Rev. B* **104**, 075147 (2021).
13. Chen, Y. *et al.* Strong correlations and orbital texture in single-layer 1T-TaSe₂. *Nat. Phys.* **16**, 218 (2020).
14. Yan, J. A., Dela Cruz, M. A., Cook, B. & Varga, K. Structural, electronic and vibrational properties of few-layer 2H- and 1T-TaSe₂. *Sci. Reports 2015 51* **5**, 1–13 (2015).
15. Wang, Z. *et al.* Surface-Limited Superconducting Phase Transition on 1T-TaS₂. *ACS Nano* **12**, 12619–12628 (2018).